Chinese Physics Letters

LETTER

Tunable Correlated Chern Insulators with Giant Magnetic Anisotropy

Cite as: Qingzhao Yao *et al*. 2026 *Chin. Phys. Lett.* **43** 060702

DOI CSTR

Recommended Articles

Quantum Anomalous Hall Effect with Tunable Chern Numbers in High-Temperature 1T-PrN_2 Monolayer

Xu-Cai Wu, Shu-Zong Li, Jun-Shan Si, Bo Huang, and Wei-Bing Zhang
Chin. Phys. Lett. **41**, (2024)

Giant Enhancement of Perpendicular Magnetic Anisotropy and Field-Free Switching Through Interfacial Engineering in Pt/Co/Pt Heterostructures

Yulin Zhang *et al*.
Chin. Phys. Lett. **43**, 030701 (2026)

Simulating a Chern Insulator with $C = \pm 2$ on Synthetic Floquet Lattice

Ling-Xiao Lei, Wei-Chen Wang, Guang-Yao Huang, Shun Hu, Xi Cao, Xin-Fang Zhang, Ming-Tang Deng, and Ping-Xing Chen
Chin. Phys. Lett. **41**, (2024)

Tuning Second Chern Number in a Four-Dimensional Topological Insulator by High-Frequency Time-Periodic Driving

Zheng-Rong Liu, Rui Chen, and Bin Zhou
Chin. Phys. Lett. **41**, (2024)

Symmetry-Driven Giant Magneto–Optical Kerr Effects in Altermagnetic Insulator

Jiaxin Luo, Xiaodong Zhou, Jinxuan Liang, Ledong Wang, Qiuyun Zhou, Yong Jiang, Wenhong Wang, Yugui Yao, Luyi Yang, and Wanjun Jiang
Chin. Phys. Lett. **43**, 020713 (2026)

iopscience.iop.org/cpl | cpl.iphy.ac.cn

A series journal of Chinese Physical Society distributed by IOP Publishing

Chinese Physics Letters

Chin. Phys. Lett. **43** 060702 (2026)

LETTER

DOI: 10.1088/0256-307X/43/6/060702
CSTR: 32039.14.0256-307X.43.6.060702

Tunable Correlated Chern Insulators with Giant Magnetic Anisotropy

Qingzhao Yao[1], Hongyan Zhao[1], Wei Xu[1], Hongguo Zhang[1], and Zhongqin Yang[1,2,*]

[1]State Key Laboratory of Surface Physics & Department of Physics, Fudan University, Shanghai 200433, China
[2]Shanghai Qi Zhi Institute, Shanghai 200030, China

[*]Corresponding author. Email: zyang@fudan.edu.cn

Achieving a high-temperature quantum anomalous Hall (QAH) effect remains an experimental challenge despite extensive research. One key limitation is the typically small magnetic anisotropy energy (MAE), generally $\leqslant$1 meV, which severely restricts the stability of long-range magnetism in two-dimensional (2D) materials. In this work, we design a monolayer LiCoTe (with ferromagnetic T_C = 535 K) from first-principles calculations. A giant MAE value of 40.4 meV is observed for LiCoTe by applying 3.5% strain. A topological transition (from the half metal to the QAH state with Chern number C = −1) as well as a large global QAH band gap (up to 266 meV) is achieved under certain strain. Based on a tight-binding model, an orbital multiplet tuning mechanism involving $d_{xz/yz}$ and $d_{x^2-y^2}$ orbitals is proposed to rationalize the giant MAE and large QAH band gap. Our findings provide a promising pathway for achieving high-temperature 2D ferromagnets and Chern insulators in real correlated materials.

Since the synthesis of two-dimensional (2D) ferromagnets $Cr_2Ge_2Te_6$ [1] and CrI_3 [2], 2D magnets have garnered significant attention due to their integrable and engineerable properties for future nanoelectronic and spintronic devices. For 2D ferromagnets, the quantum anomalous Hall (QAH) effect [3,4] has been extensively studied, because its dissipationless chiral edge current can potentially be applied to contemporary quantum electronics to overcome the grand challenges facing traditional semiconductor microelectronics. As electronic transport through chiral edge states eliminates electrical resistivity inside the samples, leaving only terminal or contact resistances, the QAH insulators, also called Chern insulators, can be employed to construct chiral interconnects in topological quantum computation and low-energy-consumption spintronic devices [5]. The utilization of the QAH effect is highly desirable at elevated temperatures, particularly room temperature; however, this remains a critical challenge. Even recent experimental observations of the QAH effect in magnetic $MnBi_2Te_4$ [6], moiré materials [7,8], and multilayer graphene heterostructures [9,10] still exhibit extremely low onset temperatures (a few K).

Over the past decade, several theoretical studies [11–15] have identified a new class of correlated materials as promising candidates for high-temperature QAH effects. Unlike Mott insulating states, which are primarily associated with strong Coulomb repulsion (U) interactions, these correlated materials are characterized by significant Hund's coupling (J) interactions arising from their multiorbital nature, in addition to intermediate U values. Hence, these materials can be classified as "Hund's metals" [16–18]. Iron-based superconductor materials (e.g., FeSe) [19–23] and ruthenates [24–28] are prototypical examples of Hund's metals. In 2024, Hund's metals were proposed as an ideal platform for QAH states for three reasons [15]: (1) Due to the inherently bad-metallic behavior of Hund's metals, topologically nontrivial band gaps around the Fermi level (E_F) can be readily induced by spin–orbit coupling (SOC) in the materials; (2) The SOC strengths of the magnetic atoms, such as Fe or Mn atoms, can be significantly enhanced by the Coulomb repulsion U [29]; (3) Extremely high ferromagnetic (FM) Curie temperatures (T_C), e.g., exceeding 1500 K as reported in Refs. [11–15] (see Table 1), can be achieved in Hund's metals due to FM double-exchange mechanisms [30–32]. These Hund's metals have, however, a fatal drawback: their absolute values of magnetic anisotropy energies (MAEs), defined as the total energy difference between in-plane (x-axis) and out-of-plane (z-axis) magnetizations, are generally very small (less than 1 meV, as shown in Table 1). This trend imposes a significant limitation on the stability of long-range FM order in 2D materials, restricting its existence to ultralow temperatures. In addition, for 2D materials with a small MAE, even a slight temperature variation can cause a deflection in the magnetization direction [33,34], potentially leading to the narrowing or complete closure of the topological band gap [35,36]. Therefore, achieving giant MAEs, largely overlooked in most previous studies of QAH states, is crucial for raising the onset temperatures of QAH effects, especially in Hund's metals.

Table 1. A summary of the typical properties of some correlated Chern insulators reported previously, including MAE, global band gaps, T_C, and Chern numbers (C).

	MAE (meV)	Band gap (meV)	T_C (K)	C
LiFeSe [11]	0.4	35	1500	2
InFeSe [12]	~0.5	403	1090	2
MgFeP [15]	~0.9	56	1525	2
FeBr [13]	~0.6	305	471	2
Fe_2IBr [14]	~0.6	~250	403	2

In this work, we propose a cobalt-based monolayer LiCoTe and demonstrate how robust QAH effects with exceptional properties can be triggered using density functional theory (DFT) calculations. The built LiCoTe monolayer exhibits dynamic stability and remains thermally stable up to 300 K. The obtained T_C of the FM ground state of LiCoTe is 535 K, much higher than room temperature. Very importantly, giant MAE values of up to 40.4 meV are obtained for LiCoTe under applied strain. A global QAH band gap up to 266 meV is achieved under certain strain with magnetization along the out-of-plane direction. The topological invariant Chern number C is tunable by strain (from C = 2 to C = −1). A tight-binding (TB) model is constructed to reveal the mechanism behind the emergence of the giant MAEs and QAH band gaps: the SOC effect is drastically enhanced due to band inversion between $d_{xz/yz}$ and $d_{x^2-y^2}$ orbitals and the orbital

Received 17 March 2026; accepted 23 April 2026; published 17 June 2026
© 2026 Chinese Physical Society and IOP Publishing Ltd. All rights, including for text and data mining, AI training, and similar technologies, are reserved.

Check for updates

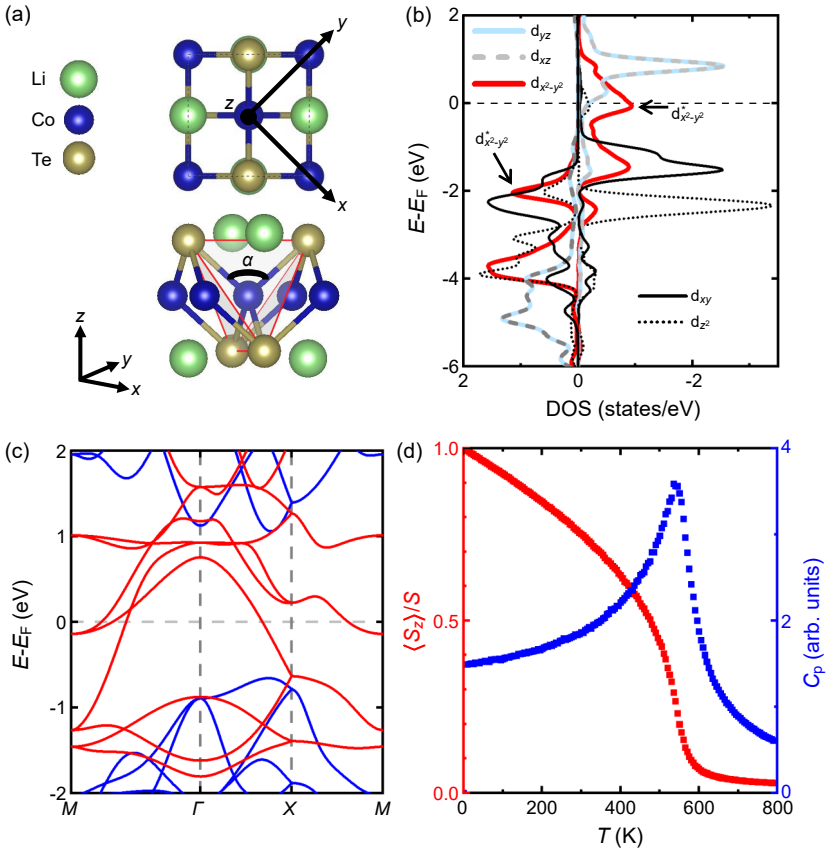

Fig. 1. Crystal and electronic structures of the designed monolayer LiCoTe. (a) Top (upper panel) and side (lower panel) views of the monolayer. (b) Partial DOSs of Co 3d orbitals in LiCoTe. The positive and negative values of the DOSs indicate the spin-up and spin-down bands, respectively. (c) Band structure of LiCoTe without SOC. The blue and red curves indicate the spin-up and spin-down bands, respectively. (d) Monte Carlo simulations for LiCoTe. Normalized $\langle S_z \rangle$ (the red curve) and heat capacity C_p (the blue curve) as a function of temperature are shown.

multiplet effect. Our results show that highly robust Chern insulators can be realized through an orbital tuning mechanism in real correlated materials.

Within the family of layered iron-based superconductor materials, the lithium-intercalated monolayer LiFeTe stands as one of the pioneering systems with the QAH effect [11]. By substituting transition metal Fe atoms with Co atoms, the valence state configuration of the magnetic ions varies from $3d^7$ to $3d^8$. Due to its multi-d-orbital characteristic, the new monolayer LiCoTe is expected to exhibit Hund's metal behaviors. As shown in Fig. 1(a), the monolayer LiCoTe has the same tetragonal structure with space group $P4/nmm$ (No. 129) as LiFeTe. The lattice parameters of the monolayer LiCoTe obtained from the DFT calculations are given in Table S1 of the Supplementary Materials (SM), and details of the DFT calculations are introduced in Part II of the SM. First-principles molecular dynamics simulations show that the monolayer LiCoTe remains intact up to a high temperature of 300 K after 10 ps [Fig. S1(a) in the SM], confirming its thermal stability. No negative frequency modes appear in the phonon spectrum [Fig. S1(b) in the SM], indicating the dynamic stability of the proposed LiCoTe monolayer.

As presented in Fig. 1(a), the $CoTe_4$ unit is a tetrahedron elongated along the z-axis, in which the bond lengths of the four Co–Te bonds are all 2.71 Å. The upward and downward Te–Co–Te bond angles α are both 96.2°, while the four lateral Te–Co–Te bond angles are enlarged due to the elongation of the $CoTe_4$ unit along the z-direction. In a regular tetrahedral crystal field Δ_{tet}, ($\alpha = 109.5°$), the five degenerate 3d orbitals split into a higher-energy triplet t_2 and a lower-energy doublet e [Fig. 2(a)]. In LiCoTe, the elongation along the z-direction of the tetrahedra causes the triplet t_2 (doublet e) to further split, according to crystal field theory [37]. Specifically, the t_2 (e) orbitals split into a higher-energy d_{xy} ($d_{x^2-y^2}$) and a lower-energy $d_{xz/yz}$ (d_{z^2}) [Fig. 2(a)]. Only the d_{xy} and d_{yz} orbitals remain degenerate. As shown in Table S1 of the SM, the next-nearest-neighbor (NNN) Co–Co bond lengths (2.85 Å) are close to the nearest-neighbor Co–Te bond lengths (2.71 Å). In addition, the Co $d_{x^2-y^2}$ orbital points directly toward the nearest Co atom [Fig. 1(a)]. Thus, the NNN Co–Co interactions through $d_{x^2-y^2}$ orbitals are significant, and are enhanced by mediation of the Te $p_{x/y}$ orbitals. As a result, the Co $d_{x^2-y^2}$ orbitals split into a bonding state $d_{x^2-y^2}$ at lower energy and an antibonding state $d^*_{x^2-y^2}$ at higher energy, as shown in Fig. 2(a). Hence, after considering the NNN Co–Te–Co (also a part of Co–Co) interactions, which are denoted as d–p–d (d–d) interactions, the antibonding state $d^*_{x^2-y^2}$ from the doublet e can become even higher in energy than the d_{xy} from the triplet t_2 [Fig. 2(a)]. The special tetrahedral crystal field effects with NNN Co-atom interactions are confirmed by DFT calculations [Figs. 2(b) and 2(c)].

When the spin polarization is taken into account in LiCoTe, the five spin-up states and the spin-down $d_{x^2-y^2}$ (almost), d_{xy}, and d_{z^2} states are occupied, as indicated in the densities of states (DOSs) of Co 3d orbitals [Fig. 1(b)]. This orbital occupation results in a magnetic moment of $2.0\mu_B$ per Co atom. In the following, we will primarily focus on the spin-down states of Co 3d, which are located around E_F. They are in an energy-level order of $d_{xz/yz} > d^*_{x^2-y^2} > d_{xy} > d_{x^2-y^2} > d_{z^2}$, different from the energy-level order discussed above based on crystal field theory. The discrepancy is removed when correlated interactions are included [see the rightmost panel in Fig. 2(a)]. The underlying reason is analyzed below. In the $CoTe_4$ tetrahedron, the Te p orbitals have strong interactions with the Co $d_{x^2-y^2}$ orbital, and this

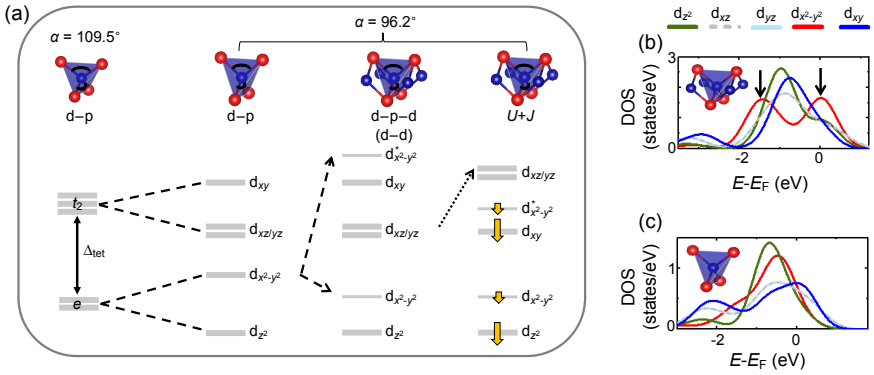

Fig. 2. The order of 3d energy levels in the monolayer LiCoTe under different interactions. (a) Schematic 3d orbital energy diagram for a $3d^8$ (Co^+) in a regular tetrahedron ($\alpha = 109.5°$) and an elongated tetrahedron ($\alpha = 96.2°$) crystal field. The Co (Te) atoms are denoted by blue (red) spheres, and the Li atoms are hidden for better visual clarity. Note that only spin-down energy levels are displayed in the rightmost panel of (a) for simplicity. (b) The DOSs of a fictitious LiCoTe monolayer, where the $CoTe_4$ units are regular tetrahedra and the lattice constant $a = 4.4$ Å. (c) The same as (b), except that the NNN Co atom in the unit cell is removed. Clearly, the bonding state $d_{x^2-y^2}$ and antibonding state $d^*_{x^2-y^2}$ are formed in (b) due to interactions from the NNN Co atoms, marked by black arrows in (b). To avoid interference from other effects, the DOSs in (b) and (c) are calculated without U, J, or spin polarization.

makes the DOS of the Co $d_{x^2-y^2}$ orbital well spread in energy in Fig. 1(b), giving itinerant behavior to the $d_{x^2-y^2}$ orbital. Oppositely, the Co $d_{xz/yz}$ orbitals exhibit clearly localized behavior. When the Coulomb repulsion U and Hund's coupling J are turned on, the spin-up (spin-down) doublet $d_{xz/yz}$ moves down (up) in energy, and a large Mott band gap opens between the occupied spin-up $d_{xz/yz}$ orbitals (lower Hubbard bands) and the unoccupied spin-down $d_{xz/yz}$ orbitals (upper Hubbard bands) [Fig. 1(b)]. The coexistence of the itinerant $d_{x^2-y^2}$ state and the localized $d_{xz/yz}$ state demonstrates that monolayer LiCoTe exhibits Hund's-metal character and is also a potential QAH candidate. While a rigorous identification of a Hund's metal typically requires more advanced dynamical mean-field theory (DMFT) [18], previous studies have shown that DFT+U and DFT+DMFT calculations yield nearly identical band structures for the correlated QAH insulator LiFeSe [11], which shares similar crystal and basic electronic structures with LiCoTe. This consistency supports the reliability of our Hund's-metal-like picture for LiCoTe. Figure 1(c) shows the band structure of monolayer LiCoTe without SOC, indicating a half-metallic band structure due to a large band gap for the spin-up states. Two spin-down bands cross around E_F, forming spin-polarized 2D Weyl points along the high-symmetry M–Γ line.

For LiCoTe, the FM structure is the magnetic ground state, which has a total energy much lower than those of the antiferromagnetic structures (Table S2 in the SM). We use Monte Carlo simulations (see Part II in the SM) to evaluate the FM T_C. The obtained T_C is 535 K [Fig. 1(d)], which is far above room temperature. The high T_C in LiCoTe can be attributed to the FM double-exchange mechanism characteristic of Hund's metals [18,30–32]: localized electrons in the $d_{xz/yz}$ bands provide local magnetic moments, and itinerant electrons in the dispersive $d_{x^2-y^2}$ bands render the material FM by hopping between different Co sites with parallel spin orientations. The total energy of LiCoTe with magnetization along the x-axis is 23.6 meV lower than that along the z-axis, giving the MAE of −23.6 meV. The SOC interaction does not significantly alter the band structure of LiCoTe [Fig. S1(c) in the SM]. The monolayer remains an FM half-metal, as the 2D Weyl point along the high-symmetry M–Γ line is protected by C_{2x} rotational symmetry.

To introduce a topological gap around E_F, the C_{2x} symmetry is broken by switching the magnetization direction from the x- to the z-axis, which can be realized via strain [Fig. 3(a)]. The strain along the z-axis is defined as $\eta = (h_0 - h)/h_0 \times 100\%$, where h (h_0) is the thickness of the monolayer [Fig. 1(a)] with (without) strain (see the thickness and optimized lattice constants in Table S3 of the SM). Figures 3(b)–3(d) [Figs. 3(e)–3(g)] show the DOSs around E_F without SOC (with SOC), respectively, under $\eta = 0.0\%$, 3.5%, and 9.4%. Only the spin-down $d_{x^2-y^2}$ and $d_{xz/yz}$ orbitals are displayed according to the above analysis. Without strain, the $d_{xz/yz}$ orbitals lie too far from E_F to induce an out-of-plane FM ground state. The $d_{x^2-y^2}$ orbital provides the dominant contribution around E_F, and the SOC interaction occurs between $d_{x^2-y^2}$ and d_{yz} (and to a lesser extent d_{xz}) orbitals. According to $\langle d_{x^2-y^2}|\hat{H}_{SOC}|d_{yz/xz}\rangle \propto |\bar{L}_{x/y}|$ [38], this type of SOC induces a nonzero orbital angular momentum $|\bar{L}_{x/y}|$ (mainly along the x-axis), as shown in Fig. 3(e). Rotating the magnetization direction of monolayer LiCoTe from the z-axis to the x-axis incurs an energy cost of 23.6 meV, indicating a giant MAE of −23.6 meV for LiCoTe in its equilibrium state. When strain is applied, figures 3(b)–3(d) show that the DOS of the antibonding state $d^*_{x^2-y^2}$ rises in energy and rapidly moves away from E_F. By contrast, the DOSs of the $d_{xz/yz}$ orbitals shift downward and cross E_F under the influence of the tetrahedral crystal field (see details in Fig. S2 of the SM). The orbital overlap between the $d_{x^2-y^2}$ and the doublet $d_{xz/yz}$ orbitals increases, reaching a maximum at $\eta = 3.5\%$ [Fig. 3(c)], and then decreases under stronger strain. Accordingly, the absolute magnitude of the MAE increases, peaks at 40.4 meV at $\eta = 3.5\%$ [Fig. 3(f)], and then decreases. Under strain $\eta = 9.4\%$, the DOS of the $d_{x^2-y^2}$ orbital is pushed away from E_F, while the DOSs of the $d_{xz/yz}$ orbitals cross and dominate near E_F [Fig. 3(d)], and SOC now occurs predominantly between d_{xz} and d_{yz} orbitals. As shown in Fig. 3(g), the DOSs of the $d_{xz/yz}$ orbitals split into two peaks flanking E_F upon inclusion of SOC. A nonzero orbital angular momentum along the z-axis is induced, according to $\langle d_{xz}|\hat{H}_{SOC}|d_{yz}\rangle \propto |\bar{L}_z|$ [38], and the total energy of system is lower by adopting an out-of-plane easy axis with an MAE of 26.0 meV.

Based on the above facts, that an out-of-plane easy axis (in-plane easy axis) arises from SOC between d_{xz} and d_{yz} ($d_{xz/yz}$ and $d_{x^2-y^2}$) orbitals, we can now clearly rationalize how the MAE of monolayer LiCoTe can be tuned by strain. Without strain, the DOSs of the doublet $d_{xz/yz}$ lie around 0.9 eV away from the E_F [Fig. 3(b)] and are thus unable to induce an out-of-plane FM ground state; however, the $d_{x^2-y^2}$ orbital near the E_F enables relatively weak SOC interactions with $d_{xz/yz}$, yielding an MAE of −23.6 meV. At $\eta = 3.5\%$, the DOSs of the doublet $d_{xz/yz}$ approach E_F, and the DOS overlap between $d_{xz/yz}$ and $d_{x^2-y^2}$ reaches its maximum, resulting in a giant MAE of −40.4 meV (the largest absolute value). The absolute value of the MAE decreases rapidly under stronger strain because the $d_{xz/yz}$ orbital is pushed away and its overlap with the $d_{xz/yz}$ orbitals diminishes. At $\eta = 5.9\%$, the DOSs of the doublet $d_{xz/yz}$ dominate the E_F, and the ground state of monolayer LiCoTe transitions to an out-of-plane FM state with a positive MAE of 20.9 meV. Thereafter, the DOS of the $d_{x^2-y^2}$ orbital continues moving away from E_F under increasing strain, and charges from the antibonding $d_{x^2-y^2}$ orbital are fully transferred to the $d_{xz/yz}$

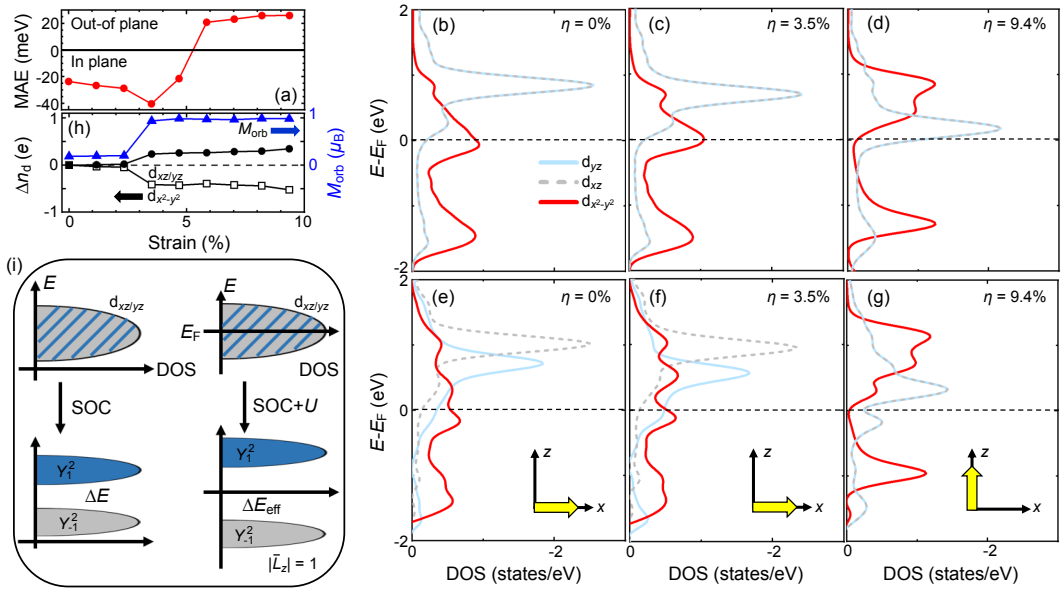

Fig. 3. Giant MAE induced by strain in the monolayer LiCoTe. (a) MAE of LiCoTe as a function of strain. (b)–(g) The spin-down partial DOSs of Co 3d orbitals in LiCoTe under strain with strengths $\eta = 0.0\%$, 3.5%, and 9.4%, respectively, (b)–(d) without SOC and (e)–(g) with SOC. In the insets of (e)–(g), the yellow arrows show the magnetization directions of the magnetic ground states for the monolayer. (h) Orbital moment M_{orb} along the z-axis and charge transfer Δn_d between the spin-down $d_{xz/yz}$ and $d_{x^2-y^2}$ orbitals as functions of strain. The charge transfer is obtained with SOC in the out-of-plane FM order. (i) The schematic diagram shows that the doublet $d_{xz/yz}$ splits into spherical harmonics $Y^2_{\pm1}$ due to the combined effects of U and SOC.

orbitals to satisfy charge conservation. Consequently, the more the $d_{xz/yz}$ DOS crosses E_F, the larger the MAE becomes. As shown in Fig. 3(a), the MAE of LiCoTe as a function of strain resembles a "V"-shaped curve: an MAE of 26.0 meV is achieved at $\eta = 9.4\%$, and an even larger MAE is expected at higher strain values along this trend.

Besides switching the magnetization direction from the x- to the z-axis in the monolayer, energy-level inversion induced by strain also drives a global topological band gap and a topological phase transition. Figures 4(a)–4(c) show the orbital-resolved band structures of LiCoTe with SOC and an out-of-plane FM order at $\eta = 0.0\%$, 2.3%, and 3.5%, respectively. Without strain, the Weyl point at E_F opens a local, topologically nontrivial band gap of only around 10 meV (see Fig. S3 in the SM). Under strain, the unoccupied $d_{xz/yz}$ bands (gray and blue bands) shift downward and meet the $d_{x^2-y^2}$ band (the red band) at the Γ point at $\eta = 2.3\%$, closing the topological band gap, as shown in Fig. 4(b). At $\eta = 3.5\%$, band inversion between the $d_{xz/yz}$ and $d_{x^2-y^2}$ bands is complete, and the $d_{xz/yz}$ bands cross E_F, reopening a global 34 meV band gap [Fig. 4(c)]. The global topological band gap increases monotonically under stronger strain, reaching 266 meV at $\eta = 9.4\%$. The topological invariant Chern number $C = (1/2\pi)\sum_n \int_{BZ} d^2\boldsymbol{k}\Omega_n(\boldsymbol{k})$, where $\Omega_n(\boldsymbol{k})$ is the Berry curvature of the nth occupied band in reciprocal space, and is calculated to identify the topology of the system. The Berry curvature $\Omega_n(\boldsymbol{k})$ is obtained via the Kubo formalism: $\Omega_n(\boldsymbol{k}) = -2\mathrm{Im}\sum_{m\neq n}[\langle\psi_{nk}|v_x|\psi_{mk}\rangle\langle\psi_{mk}|v_y|\psi_{nk}\rangle\hbar^2]/(E_m - E_n)^2$, where v_x and v_y are the velocity operators, and E_m and E_n are the eigenvalues of the Bloch states $|\psi_{mk}\rangle$ and $|\psi_{nk}\rangle$, respectively. At $\eta = 0.0\%$ ($\eta = 3.5\%$), the valence band maximum (VBM) is dominated by $d_{x^2-y^2}$ ($d_{xz/yz}$) orbitals, and the calculated Chern numbers are $C = +2$ ($C = -1$) (Fig. S3 in the SM). As a hallmark of the QAH effect, two (one) chiral edge states appear within the topological band gap for LiCoTe at $\eta = 0.0\%$ ($\eta = 3.5\%$), as shown in Fig. 4(e) [Fig. 4(f)]. Therefore, the ground state of LiCoTe transitions from a half-metal [Fig. 1(c)] with in-plane FM order to a Chern insulator [Fig. 4(c)] with out-of-plane FM order under strain.

A TB model is constructed to elucidate the mechanism behind the topological transition induced by the energy-level inversion between $d_{xz/yz}$ and $d_{x^2-y^2}$ orbitals. A 10-orbital basis set is chosen: $\{A_{x^2-y^2}, A_{xz}, A_{yz}, B_{x^2-y^2}, B_{xz}, B_{yz}, C_x, C_y, D_x, D_y\}$, where A/B and C/D represent the two inequivalent Co and ligand Te atomic sites in the unit cell, as illustrated in Fig. 1(a). The Li atoms are excluded from our TB model because they lose all their valence electrons and become bare cations (Li^+). The total Hamiltonian reads

$$H(\boldsymbol{k}) = H_{hop} + H_M + H_{SOC} = \begin{bmatrix} H_\uparrow & 0 \\ 0 & H_\downarrow \end{bmatrix} + \begin{bmatrix} H_{M\uparrow} & 0 \\ 0 & H_{M\downarrow} \end{bmatrix} + \begin{bmatrix} H_{SOC\uparrow\uparrow} & H_{SOC\uparrow\downarrow} \\ H_{SOC\downarrow\uparrow} & H_{SOC\downarrow\downarrow} \end{bmatrix}, \quad (1)$$

where H_{hop}, H_M, and H_{SOC} denote the hopping, magnetic exchange field, and on-site SOC, respectively. $H_\uparrow$ and $H_\downarrow$ represent the hopping terms in the spin-up and spin-down channels, respectively. The details are provided in Part I of the SM. As displayed in Fig. 1(b), the bands around E_F are primarily derived from the single $d_{x^2-y^2}$ orbital and the doubly degenerate $d_{xz/yz}$ orbitals. We now track the SOC-induced splitting of the $d_{xz/yz}$ doublet using spherical harmonics, which arises from the orbital multiplet effect [39] and is associated with a large MAE. The Bloch functions of the subspace spanned by these two orbitals, $|\psi\rangle = c_1|d_{xz}\rangle + c_2|d_{yz}\rangle$, can be expressed as

$$|\psi\rangle = \frac{c_1}{\sqrt{2}}\left(|Y^2_{-1}\rangle - |Y^2_1\rangle\right) + \frac{ic_2}{\sqrt{2}}\left(|Y^2_{-1}\rangle + |Y^2_1\rangle\right) = \frac{-c_1 + ic_2}{\sqrt{2}}|Y^2_1\rangle + \frac{c_1 + ic_2}{\sqrt{2}}|Y^2_{-1}\rangle. \quad (2)$$

Without SOC, the degenerate states $|Y^2_1\rangle$ and $|Y^2_{-1}\rangle$ lie above the $d_{x^2-y^2}$ orbital, as displayed in Fig. 5(a). We introduce a higher on-site energy, $\varepsilon_{x^2-y^2}$, for the $d_{x^2-y^2}$ orbital in the TB model to simulate the increased energy of the antibonding state $d^*_{x^2-y^2}$ under stronger strain, as observed in the DFT calculations. When $\varepsilon_{x^2-y^2} = -1.0$ eV, the Weyl point opens a band gap with $C = 2$ along the M–Γ path [Fig. 5(b)] under SOC. When $\varepsilon_{x^2-y^2}$ is increased to −0.85 eV, the $d_{x^2-y^2}$ band is raised and meets the $|Y^2_{-1}\rangle$ band at the Γ point, closing the band gap [Fig. 5(c)]. When $\varepsilon_{x^2-y^2}$ is increased to −0.5 eV, a topological band gap (with $C = -1$) is reopened [Fig. 5(d)]. Additionally, the doublet $d_{xz/yz}$ splits into the spherical harmonics $|Y^2_1\rangle$ and $|Y^2_{-1}\rangle$ under SOC, as illustrated in Figs. 5(b)–5(d), a phenomenon referred to as the "orbital multiplet effect" [39]. As a result, the energy of the $|Y^2_1\rangle$ state is raised by the d-orbital SOC strength λ_d, whereas that of the $|Y^2_{-1}\rangle$ state is lowered by λ_d. Finally, the $|Y^2_{-1}\rangle$ state separates from the $|Y^2_1\rangle$ state

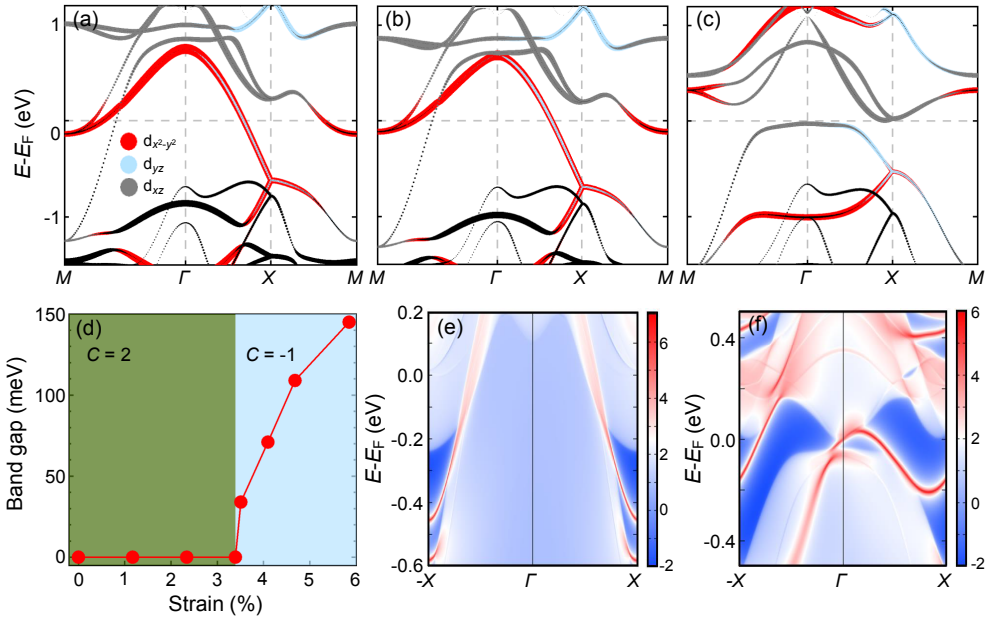

Fig. 4. The enhancement of the topological band gap in the monolayer LiCoTe in the out-of-plane FM order under compressive strain along the z-axis. (a)–(c) Orbital-resolved band structures with SOC under strain of $\eta = 0.0\%$, 2.3%, and 3.5%, respectively, where the d_{xy} and d_{z^2} contributions of Co atoms as well as the s and p contributions of Te atoms are marked in black. (d) Topological global band gaps as a function of strain, where Chern numbers C are also shown. (e) Two edge states occur in the case of (a). (f) One edge state appears in the case of (c).

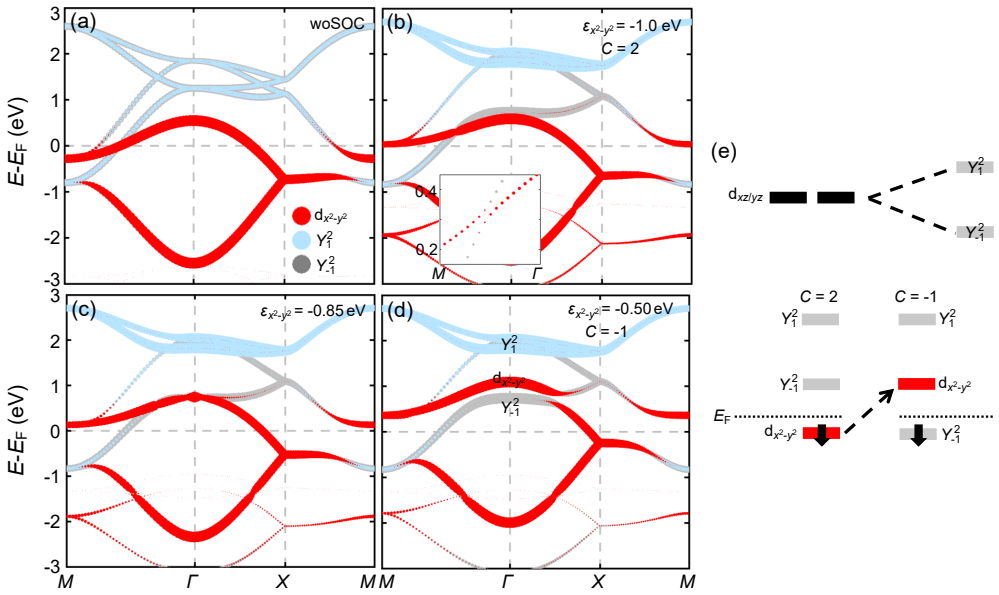

Fig. 5. Orbital-resolved band structures based on the TB model, where the doublet $d_{xz/yz}$ is expressed in terms of spherical harmonics $Y^2_{\pm 1}$. The parameters are listed in Table S4 in the SM. (a) Without SOC, the harmonics $Y^2_{\pm 1}$ remain degenerate. The on-site energy of the $d_{x^2-y^2}$ orbital is $\varepsilon_{x^2-y^2} = -1.0$ eV. (b) With SOC, a band gap along the M–Γ path (see the zoomed image in the inset) is opened, with a Chern number $C = 2$. (c) When $\varepsilon_{x^2-y^2} = -0.85$ eV, the band gap closes at the Γ point. (d) When $\varepsilon_{x^2-y^2} = -0.5$ eV, a topological band gap is reopened with $C = -1$. (e) The schematic diagram shows that the topological transition is caused by energy-level inversion between the $d_{x^2-y^2}$ and Y^2_{-1} states due to the orbital multiplet effect, where the Y^2_{-1} state is completely separated from the Y^2_1 state by SOC.

and becomes occupied, yielding a large orbital angular momentum according to $\langle Y^2_{-1}|\hat{L}_z|Y^2_{-1}\rangle = -\hbar$. This is the underlying reason for the exceptionally large MAE in LiCoTe. The topological transition mechanism of monolayer LiCoTe under strain is displayed in Fig. 5(e). With a low on-site energy $\varepsilon_{x^2-y^2}$, the energy-level order is $|Y^2_1\rangle > |Y^2_{-1}\rangle > d_{x^2-y^2}$, leading to $C = 2$, where the VBM is dominated by the $d_{x^2-y^2}$ state. With a high on-site energy $\varepsilon_{x^2-y^2}$, the energy-level order is $|Y^2_1\rangle > d_{x^2-y^2} > |Y^2_{-1}\rangle$, leading to $C = -1$, where the VBM is dominated by the $|Y^2_{-1}\rangle$ state. This trend rationalizes the topological phase transition observed in the DFT calculations (Fig. 4).

The formation of a large angular momentum is closely linked to the interplay among the occupation number, SOC, and Coulomb repulsion U within the system. The d_{xz} and d_{yz} orbitals always remain degenerate in a tetrahedral crystal field under elongation or pressure along the z-axis without SOC. Including SOC, the doublet $d_{xz/yz}$ splits into the spherical harmonics $|Y^2_1\rangle$ and $|Y^2_{-1}\rangle$, as shown in the left panel of Fig. 3(i), but this does not yield large angular momenta. If the doublet $d_{xz/yz}$ is half-filled (1/2) before including SOC [as in Fig. 3(d)], the SOC-induced splitting causes the $|Y^2_1\rangle$ and $|Y^2_{-1}\rangle$ states to become unoccupied and occupied, respectively, yielding an orbital angular momentum of $\hat{L}_z = \hbar$. Importantly, the SOC band gap ΔE can be significantly enhanced by the Coulomb repulsion U. According to the

Dudarev formula of L(S)DA+U [40], the energy contribution from the Hubbard U can be expressed in a single-particle form,

$$U_m^\sigma = U_{\text{eff}}\left(\frac{1}{2} - n_m^\sigma\right), \tag{3}$$

where $U_{\text{eff}} = U - J = 2.7$ eV is an effective value chosen for our DFT calculations, and n_m^σ denotes the occupation number of electrons in orbital m with spin channel σ. Under reasonable variations of U and J, the band dispersions and DOS around E_{F} retain their overall trend. As a result, giant MAE and topological transitions can still be triggered by strain under the interplay of the orbital multiplet effect and correlation-enhanced SOC, because the dominant contributions near E_{F} originate from the same orbital character. It should be noted that there is a subtle quantitative modification in the bandwidths, leading to a slight quantitative change in both the MAE and the critical strain for topological transitions. In the right panel of Fig. 3(i), the occupation number n_1^σ for $|Y_1^2\rangle$ is 0, while n_1^σ for $|Y_{-1}^2\rangle$ is 1, leading to a total splitting of $(1/2+1/2)U_{\text{eff}} = U_{\text{eff}}$ according to Eq. (3). This considerably increases the SOC band gap, ΔE_{eff} [Fig. 3(i)]. In the same way, if the filling of the doublet decreases from 1/2 to 0, the occupation number n_1^σ remains 0, but n_1^σ decreases from 1 to 0, leading to a reduction of the splitting from U_{eff} to 0. Thus, the doublet splitting induced by U declines with decreasing occupation and ultimately vanishes when the doublet DOSs move away from E_{F} [left panel in Fig. 3(i)]. Clearly, the SOC effect is drastically enhanced by U only when the doublet DOSs cross E_{F} [Figs. 3(b)–3(g)], thus enabling the emergence of large angular momenta.

As analyzed above, accompanying the topological transition from $C = 2$ to $C = -1$ [Fig. 4(d)], charge transfer occurs between the $d_{x^2-y^2}$ and $d_{xz/yz}$ orbitals, with the $d_{x^2-y^2}$ orbital losing charge to the $d_{xz/yz}$ orbitals under certain strain. The DFT results of the charge transfer between the orbitals as a function of strain are illustrated in Fig. 3(h). The doublet $d_{xz/yz}$ is nearly unoccupied without strain and gains 0.70 electrons under $\eta = 9.4\%$. According to the orbital multiplet effect as presented in Fig. 3(i), a giant angular momentum $|\bar{L}_z|$ and thus a much larger orbital moment M_{orb} along the z-axis will be induced via SOC+U. As indicated in Fig. 3(h), the orbital moment M_{orb} is directly proportional to the charge gained by the doublet $d_{xz/yz}$, increasing from $0.19\mu_{\text{B}}$ (without strain) to $0.99\mu_{\text{B}}$ at $\eta = 9.4\%$. Hence, the DFT calculations are in good agreement with the theoretical evaluation $\langle Y_{-1}^2|\hat{L}_z|Y_{-1}^2\rangle = -1\hbar$. The orbital moment ($0.99\mu_{\text{B}}$) achieved in the monolayer LiCoTe is more than one order of magnitude larger than that of Mn_3Ge [41], where the orbital moment plays a crucial role in the experimental observation of the anomalous Hall effect in Mn_3Ge [42]. Besides the orbital moment M_{orb} and MAE, the mechanism behind the monotonic increase of the SOC band gaps under strain [Fig. 4(d)] can also be revealed now. For the doublet $d_{xz/yz}$, its effective SOC band gap can be written as [29]

$$\Delta E_{\text{eff}} \approx \Delta E_0 + U_{\text{eff}}\frac{|\bar{L}_z|}{\hbar}. \tag{4}$$

And the orbital angular momentum is

$$|\bar{L}_z| = |\langle Y_1^2|\hat{L}_z|Y_1^2\rangle + \langle Y_{-1}^2|\hat{L}_z|Y_{-1}^2\rangle| = \hbar n_{-1}^\sigma, \tag{5}$$

where n_{-1}^σ is the occupation number for $|Y_{-1}^2\rangle$ state and the occupation number n_1^σ for $|Y_1^2\rangle$ state is 0. By combining Eqs. (4) and (5), we can find the relationship between the doublet $d_{xz/yz}$ SOC band gap and its occupation as

$$\Delta E_{\text{eff}} \approx \Delta E_0 + U_{\text{eff}} n_{-1}^\sigma. \tag{6}$$

The doublet $d_{xz/yz}$ continues to gain charge when $\eta \geqslant 3.5\%$ [Fig. 3(h)], resulting in the monotonic increase of the SOC band gap [Fig. 4(d)]. As indicated in Fig. 4(d), a relatively large strain (3.5%) is required to induce the topological phase transition in the monolayer LiCoTe. Its structural stability under large strain is confirmed by its phonon spectrum at strain $\eta = 9.4\%$ [Fig. S1(d) in the SM]. In experiments, the out-of-plane uniaxial strain in 2D materials can be realized using established techniques, such as scanning electron microscopy-based manipulation [43] and diamond anvil cell-based high-pressure methods [44], which have been well demonstrated in previous studies. Experimental studies have also demonstrated that 2D materials can usually possess exceptional mechanical stability under substantial strain. For instance, monolayer MoS_2 and graphene can withstand strain ranging from 6% to 11% [45] and up to 25% [46], respectively. However, considering that LiCoTe is an atomically thin monolayer and that dynamical stability does not guarantee experimental realizability, achieving such a large out-of-plane strain may remain challenging in practice.

In conclusion, we propose a rare correlated Chern insulator with giant magnetic anisotropy in monolayer LiCoTe from DFT calculations and TB models. The proposed LiCoTe exhibits both thermal and dynamical stability, along with a high FM T_{C} (535 K). An extremely high MAE value of up to 40.4 meV is observed for the material upon applying 3.5% strain. A topological transition from Chern number $C = 2$ to $C = -1$, together with global QAH band gaps (up to 266 meV), can be achieved under certain strain. The giant MAE, large QAH band gap, and substantial orbital angular momentum ($M_{\text{orb}} = 0.99\mu_{\text{B}}$) in the monolayer can be well understood through an orbital multiplet mechanism involving the $d_{xz/yz}$ orbitals after their inversion with the $d_{x^2-y^2}$ orbital. The interplay among the occupation number, SOC, and Coulomb repulsion U governs the emergence of the orbital multiplet effect. Our work paves the way for applications in topological quantum computation, spintronic devices, and permanent magnets with giant MAEs in correlated 2D materials.

Acknowledgements

This work was supported by the National Natural Science Foundation of China (Grant Nos. 12574254 and 12174059). The calculations were performed at the High Performance Computational Center (HPCC) of the Department of Physics at Fudan University. We thank Dr. Xinyuan Wei for assistance in cluster software optimization and technical support.

References

[1] Gong C, Li L, Li Z L *et al*. 2017 *Nature* **546** 265
[2] Huang B, Clark G, Moratalla E N *et al*. 2017 *Nature* **546** 270
[3] HaldaneF D M 2017 *Rev. Mod. Phys.* **89** 040502
[4] Chang C Z, Liu C X, and MacDonald A H 2023 *Rev. Mod. Phys.* **95** 011002
[5] Zhang X and Zhang S C 2012 *Proc. SPIE Micro-Nanotechnol. Sens. Syst. Appl. IV* **8373** 837309
[6] Deng Y, Yu Y, Shi M Z *et al*. 2020 *Science* **367** 895
[7] Serlin M, Tschirhart C L, Polshyn H *et al*. 2020 *Science* **367** 900
[8] Li T, Jiang S, Shen B *et al*. 2021 *Nature* **600** 641
[9] Sha Y, Zheng J, Liu K *et al*. 2024 *Science* **384** 414
[10] Han T, Lu Z, Yao Y *et al*. 2024 *Science* **384** 647
[11] Li Y, Li J, Li Y *et al*. 2020 *Phys. Rev. Lett.* **125** 086401
[12] Huan H, Xue Y, Zhao B *et al*. 2022 *Phys. Rev. B* **106** 125404
[13] Guo S D, Zhu Y T, Xin J L *et al*. 2022 *J. Mater. Chem. C* **10** 8381
[14] Guo S D, Mu W Q, Xiao X B *et al*. 2021 *Nanoscale* **13** 12956
[15] Yao Q Z, Xue Y, Zhao B *et al*. 2024 *Nano Lett.* **24** 1563
[16] Georges A, de'Medici L, and Mravlje J 2013 *Annu. Rev. Condens. Matter Phys.* **4** 137
[17] Bascones E, Valenzuela B, and Calderón M J 2016 *C. R. Phys.* **17** 36
[18] Stadler K M, Kotliar G, Weichselbaum A *et al*. 2019 *Ann. Phys.* **405** 365
[19] Kostin A, Sprau P O, KreiselA *et al*. 2018 *Nat. Mater.* **17** 869
[20] Yu R, Hu H, Nica E M *et al*. 2021 *Front. Phys.* **9** 578347
[21] de'Medici L, Giovannetti G, and Capone M 2014 *Phys. Rev. Lett.* **112** 177001
[22] Arribi P V and de'Medici L 2021 *Phys. Rev. B* **104** 125130
[23] Craco L and Leoni S 2021 *Phys. Rev. B* **103** 075110
[24] Sutter D, FatuzzoC G, Moser S *et al*. 2017 *Nat. Commun.* **8** 15176
[25] Nakayama M, Kondo T, KurodaK *et al*. 2018 *Phys. Rev. B* **98** 161102
[26] Sutter D, Kim M, Matt C E *et al*. 2019 *Phys. Rev. B* **99** 121115
[27] Kim M, Kwon J, Kim C H *et al*. 2022 *Npj Quantum Mater.* **7** 59
[28] Deng X, Stadler K M, Haule K *et al*. 2019 *Nat. Commun.* **10** 2721

[29] Li J, Yao Q, Wu L *et al*. 2022 *Nat. Commun.* **13** 919
[30] KorotinM A, Anisimov V I, Khomskii D I *et al*. 1998 *Phys. Rev. Lett.* **80** 4305
[31] Biermann S, de'Medici L, and Georges A 2005 *Phys. Rev. Lett.* **95** 206401
[32] Streltsov S V and KhomskiiD I 2017 *Phys. Usp.* **60** 1121
[33] Allenspach R and Bischof A 1992 *Phys. Rev. Lett.* **69** 3385
[34] Miyashita S, Nishino M, TogaY *et al*. 2021 *Sci. Technol. Adv. Mater.* **22** 658
[35] Li Z, Han Y, and Qiao Z 2022 *Phys. Rev. Lett.* **129** 036801
[36] Shu J, Zhao X, Fan W *et al*. 2025 *Phys. Chem. Solids* **199** 112552
[37] KhomskiiD I 2014 *Transition Metal Compounds* (Cambridge Univ Press, Cambridge, UK)
[38] Dai D, Xiang H, and Whangbo M H 2008 *J. Comput. Chem.* **29** 2187
[39] Ou X, Wang H, Fan F *et al*. 2015 *Phys. Rev. Lett.* **115** 257201
[40] Dudarev S L, Botton G A, Savrasov S Y *et al*. 1998 *Phys. Rev. B* **57** 1505
[41] Chen H, Wang T C, Xiao D *et al*. 2020 *Phys. Rev. B* **101** 104418
[42] Nayak A K, Fischer J E, Sun Y *et al*. 2016 *Sci. Adv.* **2** e1501870
[43] Wang B, Li J, Fang Z *et al*. 2024 *Nano Lett.* **24** 4965
[44] Chang X, Liu J, Tao Y *et al*. 2025 *Inorg. Chem.* **64** 14989
[45] Bertolazzi S, Brivio J, and Kis A 2011 *ACS Nano* **5** 9703
[46] Kim K S, Zhao Y, Jang H *et al*. 2009 *Nature* **457** 706